ADVANCED MATERIALS
www.advmat.de

Ultrastrong Boron Frameworks in ZrB_{12}: A Highway for Electron Conducting

Teng Ma, Hui Li, Xu Zheng, Shanmin Wang, Xiancheng Wang, Huaizhou Zhao, Songbai Han, Jian Liu, Ruifeng Zhang, Pinwen Zhu,* Youwen Long, Jinguang Cheng, Yanming Ma, Yusheng Zhao, Changqing Jin, and Xiaohui Yu**

Hard and superhard materials have brought substantial interest because of their wide range of technological applications in industry and fundamental importance in condensed-matter physics.[1–3] In conventional design of the intrinsically superhard materials such as diamond and cubic boron nitride (cBN), the pure covalent bonding network based on B—C—N—O systems is believed to provide both the high incompressibility (i.e., high bulk modulus) and the high resistance to plastic deformation manifested with high hardness.[4,5] However, such pure localized covalence bonds are unfavorable for electron transport, leading to large band gaps in those material systems characterized as insulators. The electrical resistivity of diamond and cBN, for example, is as high as $\approx 10^{18}$ Ω•m, which severely limits their diverse applications such as electronic applications under working condition of high stress (e.g., hard coatings used in electromechanical systems, anvils of large volume press, etc.). In this sense, the synthesis of novel superhard materials with high electrical conductivity has been an urgent task, calling for more experimental effort along this direction.

During last decade, the borides of transition metals (TM) have evoked much attention,[6–12] because some of them have been thought to be potential candidates of superhard materials with excellent electrical conductivity as proposed by Kaner et al.[6] This is not unexpected because the transition metal possesses high density of valence electrons and often leads to highly elastically incompressible compounds. In addition, the formation of strong covalent, 3D boron—boron bonding networks can significantly enhance the resistance to plastic deformation.[7] As commonly accepted, the hardness of TM borides increases with the boron content incorporated in the parent metal, owing to the formation of strong covalent TM—B and B—B bonding networks. Such correlation, although still under debate, appears to hold well for some TM triborides and tetraborides, including WB_3 (originally reported as WB_4),[8,9] FeB_4,[10] and CrB_4,[11,12] exhibiting excellent hardness exceeding to their diboride counterparts. On the other hand, the metallic feature of some TM borides is mainly attributed to the TM—TM bonding for transporting electrons freely. However, such metallic bonds are mechanically weaker than the B—B bonds and unfavorable for achieving high hardness, due to the low resistance of metallic bonds against shear deformation.

To the best of our knowledge, it is still challenging to synthesize TM boride with both high hardness and high electrical conductivity through increasing of boron content, especially for borides in a B:TM molar ratio exceeding 4:1. This is because the mobility of d-electrons of the compounds would readily be suppressed, owing to the extended hybridization between valence orbitals of TM and 2p orbitals of boron. Tetraborides (TMB_4) (such as CrB_4[10] and MoB_4[13]) are typical examples, which exhibit sufficiently enhanced resistivity of a few orders of magnitude greater than that of their monoboride or diboride counterparts. From this point of view, further increase of boron content would open up a band gap in the corresponding TM boride, giving rise to semiconductors or insulators. In this work, we have systematically investigated ZrB_{12}, one of boron-rich TM borides. Contrary to what one might expect, this boride exhibits extremely high electrical conductivity with high hardness. Both superior conductivity and hardness of ZrB_{12} are closely associated with the extended B—B 3D covalent bonding network as it is not only favorable for achieving high hardness, but also provides conducting channels for transporting valence electrons.

Figure 1a shows a polyhedral view of crystal structure of ZrB_{12}. The crystal structure can well be refined with space

T. Ma, Dr. H. Li, X. Zheng, Dr. X. Wang, Dr. H. Zhao, J. Liu, Prof. Y. Long, Prof. J. Cheng, Prof. C. Jin, Dr. X. Yu
Beijing National Laboratory for Condensed Matter Physics
Institute of Physics
Chinese Academy of Sciences
Beijing 100190, China
E-mail: yuxh@iphy.ac.cn

T. Ma, Prof. P. Zhu, Prof. Y. Ma
State Key Laboratory of Superhard Materials
College of Physics
Jilin University
Changchun 130012, China
E-mail: zhupw@jlu.edu.cn

Prof. S. Wang, Prof. Y. Zhao
Department of Physics
South University of Science and Technology of China
Shenzhen 518055, China

Prof. Y. Long, Prof. C. Jin
Collaborative Innovation Center of Quantum Matter
Beijing 100190, China

Dr. S. Han
Neutron Scattering Laboratory
China Institute of Atomic Energy
Beijing 102413, China

Prof. R. Zhang
School of Materials Science and Engineering
Beihang University
Beijing 100191, China
E-mail: zrf@buaa.edu.cn

DOI: 10.1002/adma.201604003

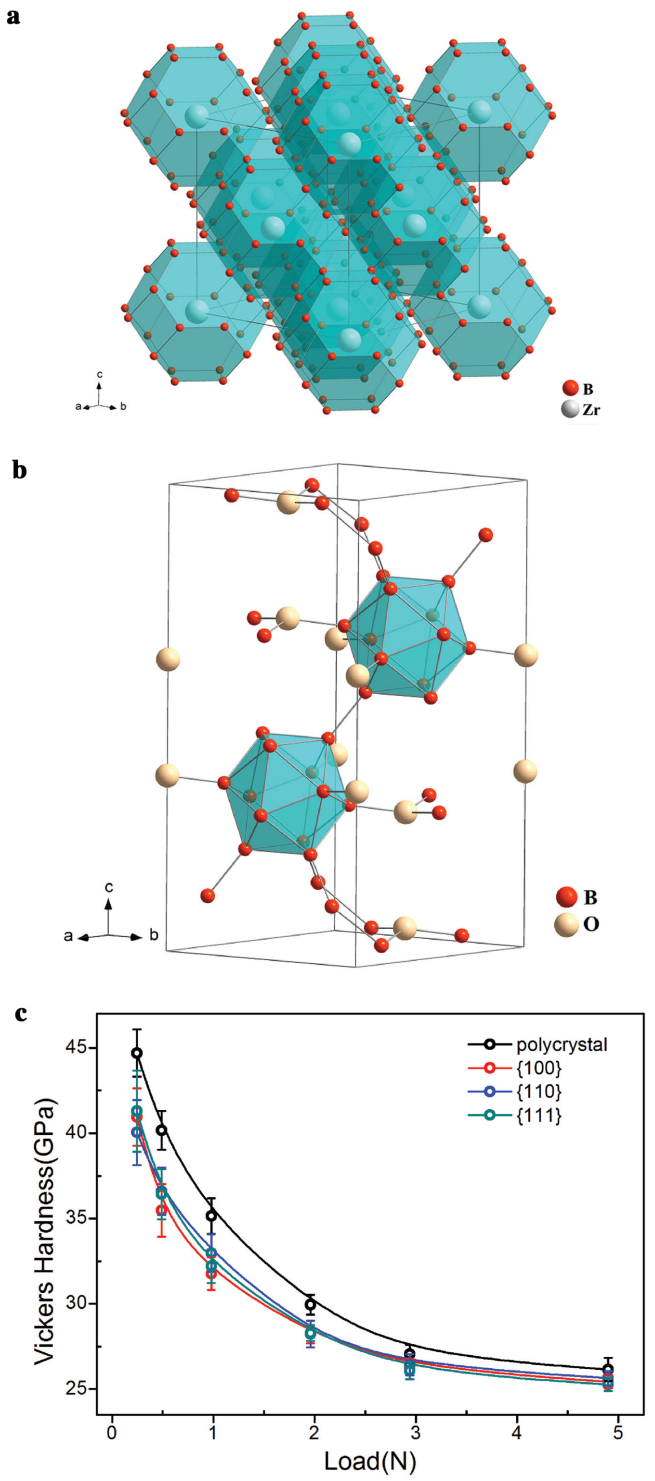

Figure 1. a) A polyhedral view of the crystal structure of orthorhombic ZrB_{12}. b) The crystal structure of rhombohedral B_6O. c) Measured Vickers hardness as a function of applied loads from 0.25 to 4.9 N.

group of Fm3m (No. 225), using X-ray diffraction (XRD) data. The refined structural details are summarized in Table S1 in the Supporting Information and the refined XRD patterns are plotted in Figure S1 in the Supporting Information. As shown in Figure 1a, the crystal structure of ZrB_{12} is composed of $\{ZrB_{24}\}$ clusters with Zr atom sitting in the vacancy of corner-truncated octahedron $\{B_{24}\}$. Remarkably, the compound exhibits a 3D bonding network between TM and boron, which is structurally more favorable than hexagonal and orthorhombic TMB_x (x = 1–4) for producing mechanically isotropic borides. Furthermore, the refined B—B bond distances are 1.68 and 1.78 Å, which are shorter than those in WB_3 and ReB_2, indicating a high hardness of ZrB_{12}.[8,14] In addition, it can be seen that the crystal structure of ZrB_{12} contains the similar B_{12} clusters as B_6O which is a superhard material with an R-3m crystal structure (Figure 1b). The major difference is the inclusion of Zr at the center of boron cluster in $\{B_{24}\}$, which may modify the mechanical and electrical properties as will be discussed in the latter sections.

To determine the hardness of ZrB_{12}, the Vickers hardness measurements were performed on well-sintered polycrystalline bulk samples prepared under high pressure (P) and high temperature (T) condition of 6 GPa and 2300 K. The single-crystal samples were also grown for examining crystallographic orientation dependence of hardness. Figure 1c shows the determined polycrystalline Vickers hardness, Hv, as a function of applied load. Under the load of 0.49 N, the determined Hv value of ZrB_{12} is 40 (1) GPa, which is comparable to that of ReB_2 (≈38 GPa)[14] and WB_4 (≈43 GPa) under the same load.[8] According to the criterion proposed by Kaner and co-workers, superhardness can be defined under a relatively low load of 0.49 N, based on which, ReB_2, WB_4, and recently $W_{1-x}Ta_xB$ have all been considered as superhard materials.[8,15,16] In this standard, ZrB_{12} should be another boride with super hardness. On the other hand, with the increasing load, the hardness decreases gradually and approaches an asymptotic value of ≈27 GPa at 4.9 N, still higher than that of ReB_2 (26.6 and 20.0 GPa reported by different groups[17,18]) and WB_4 (25.5 GPa[19]). It should be mentioned that the asymptotic Hv values of all these borides are less than 40 GPa, the traditional threshold for superhard material.[20] At present, it is still challenging to synthesize the pure phase WB_3 and MoB_3, however, the theoretical calculations reveal that WB_3 and MoB_3 show much lower indentation strength than that of ReB_2.[21] Besides, the measurements of the Vickers hardness on single crystal ZrB_{12} show isotropic property on the {100}, {110}, {111} planes, which should be due to the high symmetric frameworks formed by B–B clusters. In contrast, most of TM diborides (e.g., OsB_2 and ReB_2) adopt a hexagonal symmetry with layered stacking of alternating TM layers and B dimers along c-axis, leading to structurally anisotropic hard/superhard borides.

The phase stability and compressibility of ZrB_{12} were investigated by synchrotron XRD in a diamond-anvil cell (DAC). The cubic ZrB_{12} is structurally stable up to 43 GPa and no phase transition was observed. The bulk modulus, B_0, of ZrB_{12} is calculated by fitting the derived pressure–volume data to the second order Birch–Murnaghan equation of state (see Figure S2 in the Supporting Information). The thus-obtained B_0 value is 221 (8) GPa at $B'_0 = \partial B/\partial P \approx 4$ (see Figure S2 in the Supporting Information). Interestingly, such value in ZrB_{12} is slightly lower than that of B_6O, B_v = 270[22] and 230 GPa,[23] but much lower than that of ReB_2, WB_4, and CrB_4 with a lower concentration of boron, because the bulk modulus is mainly attributed to the

Adv. Mater. 2016,
DOI: 10.1002/adma.201604003

valence-electron density of transition metals. Although ZrB_{12} has a relatively low elastic bulk modulus, it shows a superior hardness rivaling or even exceeding fore-mentioned borides, because the hardness ultimately measures the plastic deformation under indentations. [24]

In order to underline the physical origin of high hardness of ZrB_{12}, we have performed the first principle calculations on elastic properties by means of an efficient strain-energy method.[25] Our calculated lattice constant of cubic ZrB_{12} (a = 7.402 Å) is in good agreement with our experimental value (a = 7.409 Å[26]). Our obtained elastic constants of ZrB_{12} are C_{11} = 403 GPa, C_{12} = 152 GPa, C_{44} = 248 GPa, and the derived Voigt bulk modulus B_v = 236 GPa, shear modulus G_v = 199 GPa, and Poison ratio ν = 0.171, being in agreement with the previous experimental and theoretical values.[26] It is seen that the bulk and shear moduli are comparable to those of B_6O (B_v = 227 GPa)[27] in which similar 3D covalent bond network consisting of boron cage is believed to be responsible to the high hardness of B_6O. It can be however found that, the introduction of Zr atoms into cuboctahedral B_{12} cage slightly increase the bulk modulus, but decrease the shear modulus from 211 GPa for B_6O to 199 GPa for ZrB_{12}, indicating a stronger rigidity for the former case.

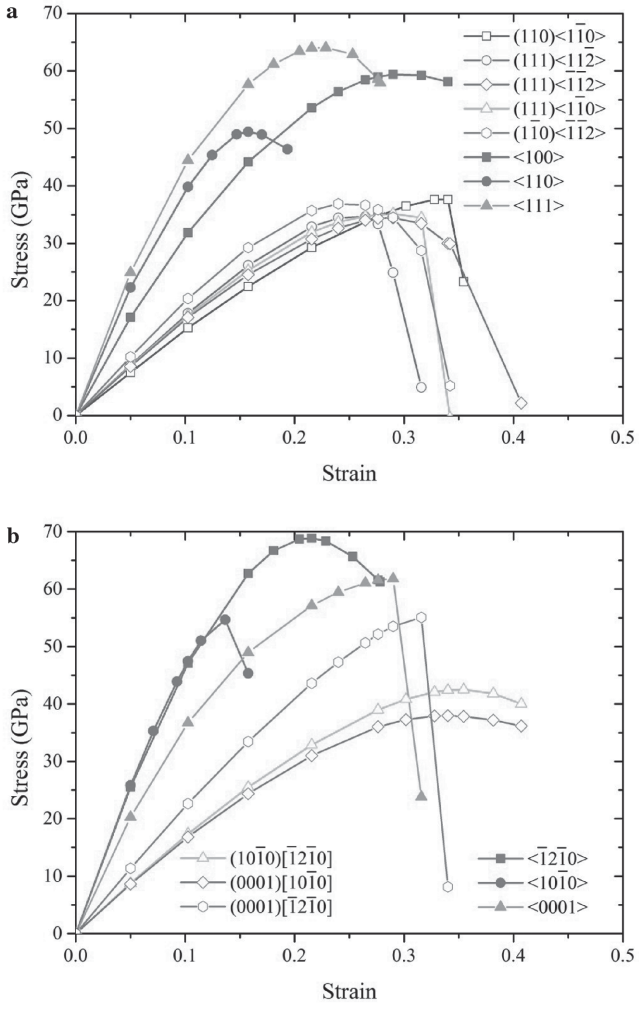

Figure 2. The calculated stress–strain relationships for a) ZrB_{12} and b) B_6O under various loading conditions.

It is generally believed that high elastic moduli do not guarantee a high mechanical strength.[24] The anisotropic ideal shear strength of ZrB_{12} is accordingly derived from the calculated stress–strain relationships along different slip systems which are presented in **Figure 2**a, and in comparison, Figure 2b presents the calculated results for superhard B_6O. It is seen that the shear strengths of ZrB_{12} are nearly isotropic within {111} planes with the minimum value of 34.5 GPa appearing along {111} [–1–12] deformation path, which is comparable to that of ReB_2 (34.4 GPa), WB_3 (37.7 GPa), and B_6O (38 GPa).[28] Such results are in consistency with our experiments in which the asymptotic Vickers hardness of ZrB_{12} (≈27 GPa) is only comparable to, if not lower than, those of ReB_2 (26.6 GPa) reported by Gu et al., WB_3 (25.5 GPa) by Tao et al. and of $W_{1-x}Ta_xB$ by Yeung et al.[16–19] The hardness of these transition metal borides are however lower than those of B_6O (45 GPa) and cBN (48 GPa), which can be attributed to their relatively lower shear strength with unique deformation path. The anisotropy of the shear strength along the selected five slip systems is estimated as $\tau_{(110)\langle 1\text{–}10\rangle}:\tau_{(1\text{–}10)\langle -1\text{–}12\rangle}:\tau_{(111)\langle 11\text{–}2\rangle}:\tau_{(111)\langle -1\text{–}12\rangle}:\tau_{(111)\langle 1\text{–}10\rangle}$ = 37.7:36.9:34.6:34.5:35.2, indicating an isotropic feature. Since the ideal shear strength is closely related to the slip resistance to dislocations via Peierls–Nabarro stress,[29] our theoretical result of the ideal shear strengths shows agreement with the determined isotropic feature of hardness on the {100}, {110}, {111} planes. Figure S3 in the Supporting Information presents the deformation paths of ZrB_{12} upon shearing along the {111} [–1–12] slip system before and after lattice instability. It is shown that the boron cage carries the plastic deformation by a recombination of surrounding B—B covalent bond networks. This does not resemble the observed lattice instability mode of B_6O along the weakest shearing mode,[24] in which the B—B bonds that connect the boron cage are responsible for the lattice instability and consequently carry the plastic flow during shearing. This suggests that the introduction of Zr atom within boron cage will modify the deformation paths, and slightly decrease the shear plastic resistance of boron cage as compared to B_6O. This provides an atomistic explanation why our experimentally determined hardness of ZrB_{12} is slightly lower than that of B_6O.

In order to gain a deeper understanding into the physical origin of the mechanical properties for ZrB_{12}, the valence charge density (VCD) and valence charge density difference (VCDD) are calculated for ZrB_{12} and shown in Figure S4 in the Supporting Information. It is qualitatively seen that the strong symmetrical B—B directional covalent bond network in ZrB_{12} structure suggests significant electron localization there, and the polarization of valence charge density around Zr atoms (revealed by the contour shape in the cross section plot of VCDD) is believed to be responsible for the mechanical strength and deformation paths under shear stress. It is concluded that the high symmetrical electronic partition and localization should be responsible for the high value of hardness for ZrB_{12}, albeit it does not exceed B_6O.

To study electron transport properties of ZrB_{12}, the electrical resistivity (ρ) measurement was carried out on (110),

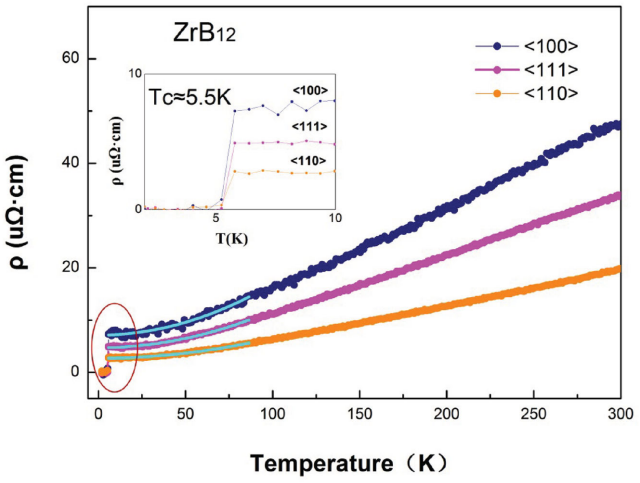

Figure 3. Electrical resistivity measurement of ZrB_{12} from 300 to 2 K. The inset shows the fitting of electrical resistivity from 6 to 60 K.

(111), and (100) planes, respectively, on the basis of a single-crystal sample. The measured ρ–T data is plotted in **Figure 3** for all these planes. A clearly sharp resistivity drop occurs at T_c = 5.5 K, indicating superconducting transition in this compound, which agrees well with previously reported result.[30] The residual resistivity, ρ_0, is extrapolated from a fit of the data to $\rho = \rho_0 + aT^2$ (where T and a are temperature and constant, respectively). The thus-derived values for (110), (111), and (100) planes for single crystal ZrB_{12} in our experiment are 2.7, 4.7, and 7.1 μΩ cm, respectively, which is in good agreement with previously reported value on polycrystalline ZrB_{12} sample (with small amount of ZrB_2 as impurity) by Gasparov et al.[31] The residual resistivity ratio (i.e., defined as ρ_{300K}/ρ_0) is around 7. It is worthwhile to mentioned that the room-temperature resistivity of (110) plane is small (only 18 μΩ cm) and very close to that of platinum metal (Pt), suggesting excellent conductivity. The similar high conductivity has also been found in most TM monoborides and diborides (such as CrB, WB, OsB_2, and ReB_2) as a result of alternating stacking of metal layer and boron dimer in these hexagonal compounds.[32] Apparently, the metal—metal bonding layers provide a natural channel for transporting electrons, leading to high electronic conductivity in these borides with low concentration of boron. The ρ of CrB, for example,[32] is as low as ≈45 μΩ cm at room temperature. Interestingly, the increasing boron concentration increases the resistivity up to ≈520 μΩ cm in orthorhombic CrB_4,[10] one order of magnitude larger than that in CrB, probably because of the destruction of electron transporting channels (i.e., layer stacking of metal atoms) in orthorhombic phase. As a result, more electrons of Cr are involved in the hybridization with boron.

In the case of ZrB_{12}, the Zr atoms are constrained in the B–B truncated octahedrons, the distance between two nearest-neighboring Zr atoms (5.2 Å) is much larger than its Van der Waals diameter (3.2 Å), indicating the valence electrons cannot freely parade between Zr atoms. Surprisingly, the ZrB_{12} possesses such a low electrical resistivity ≈18 μΩ·cm at room temperature (RT), which is only 40% of CrB and OsB_2 and comparable to that of Pt ≈20 μΩ ·cm at RT. Furthermore, the Seebeck coefficient of ZrB_{12} is only 2.0 μV·K^{-1} at RT, which is also comparable to that of Cu and Pt, and could identify its excellent electrical transport behaviors as a metallic conductor.

To better understand the high conductivity of ZrB_{12}, we calculate the electronic structure of ZrB_{12}. The projected electronic density of states (PDOS) shows bulk ZrB_{12} is metallic (**Figure 4**a), and the conduction bands at the Fermi level are hybrid states mainly composed by B-2p (red line in Figure 4a) and Zr-4d (green line in Figure 4a) orbitals. Such result is consistent to the pioneers' calculation done by Thakur et al., who use the X-ray photoelectron spectroscopy (XPS) techniques combined with density functional theory (DFT) calculations to map out the electronic structure of ZrB_{12}.[33] The Bader charge analysis shows ≈2.6 electrons of each Zr atom transfer from Zr-4d to B-2p orbital, and each B atom gains ≈0.2 electrons. Twelve intersections between conduction bands and the Fermi surface are found throughout all the symmetrical pathways in the first Brillouin zone, as shown in Figure 4b. Because the conductivity is relevant to the energy bands at the Fermi level, we plot the spatial distributions of band decomposed charge density (PBDC) at all these intersections in real space (Figure 4c–f). Two types of B—B bonds are found based on the symmetry of orbital overlapping, which are the σ-bond formed by head-on overlapping, and the π-bond formed by two lobes overlapping. It is interesting to see the B–B connection between adjacent B_{12} motifs can act as a bridge for two nearest Zr atoms, which can be called as Zr–BB–Zr bridge (represented by red rectangle in Figure 4c). The distributions of PBDC for the Zr–BB–Zr bridge at the Fermi level can be divided into four kinds of delocalized states, which are composed by Zr 4d and B—B σ-bond orbitals (Figure 4c), B—B π-bond orbitals (Figure 4d), Zr 4d and B—B π-bond orbitals (Figure 4e), Zr 4d and B—B π^*-bond orbitals (Figure 4f), respectively. It is noted the intersection at Γ–X pathway (Figure 4e) is the most dispersive state, in which the B—B π-bond and Zr-4d orbitals form delocalized channels for conducting valence electrons. Each Zr atom can form conducting channels to 12 vicinal Zr atoms (in O_h symmetry), leading to a high-symmetrical conducting network extended to the whole ZrB_{12} crystal. To explore the strength of this Zr—B bond, we employed the Lobster code[34–36] to do the Crystal Orbital Hamilton Populations (COHP) analysis for ZrB_{12}, and the results are shown in Figure S5 in the Supporting Information. The COHP displays Zr-4p and B-2p orbitals strongly overlap at the Fermi level, forming bonding interaction (Figure S5a, Supporting Information). Similarly, B–B pair is also within bonding energy region at the Fermi level (Figure S5b, Supporting Information). According to the COHP, both Zr–B and B–B pairs have significant overlapping at Fermi level, in consistence to previous analysis. Therefore, based on DFT calculation, we have confirmed the B—B π-bond and Zr 4d orbital can form highly dispersive bands, making ZrB_{12} a great conductor. Based on the DFT calculated electronic structure, we further study the electronic transport properties of ZrB_{12}, the Seebeck coefficient as a function of the temperature is calculated at intrinsic condition (Figure S6b, Supporting Information). We observe the absolute value of Seebeck coefficient is extremely small (≈3 μV·K^{-1} at 300 K), comparable to experimental result (≈2 μV·K^{-1}), indicating the excellent metallic feature of ZrB_{12}. It is surprising that the calculated

Adv. Mater. 2016,
DOI: 10.1002/adma.201604003

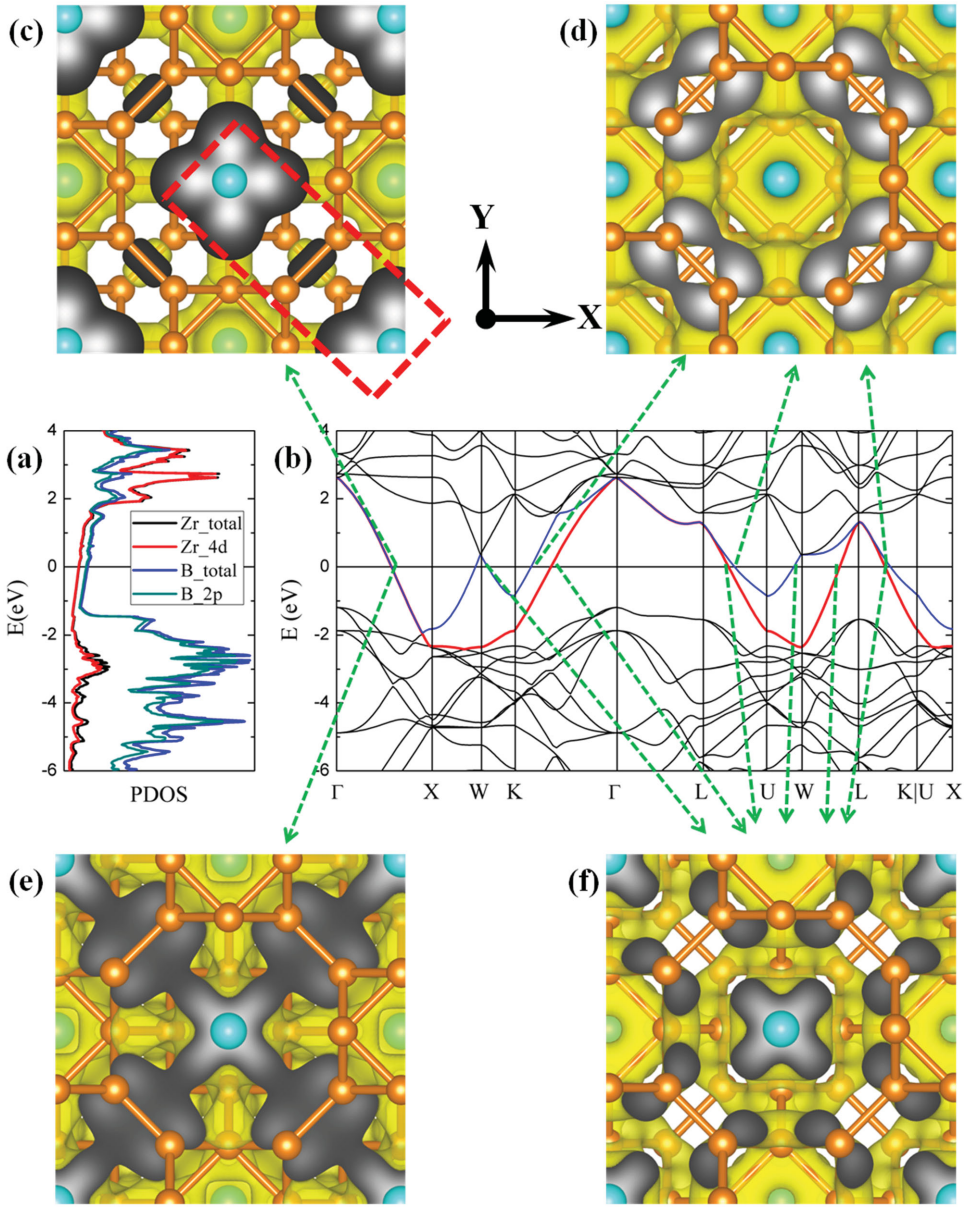

Figure 4. a) PDOS for ZrB_{12}. b) Band structures of ZrB_{12} around the Fermi level. The red (band 21) and blue (band 22) lines denote to the two bands crossing the Fermi level, respectively. c–f) The distributions of partial band decomposed charge density (isovalue = 0.0035 $Å^{-3}$) at various *k*-points at the intersections between conduction bands and the Fermi level (directed by the green arrows). Color code: Zr (large blue ball), B (small orange ball), Charge density (yellow surface and gray scaled section). The atomic models and charge density are visualized by VESTA3 package. The red rectangle in Figure 1c denotes to the Zr–BB–Zr Bridge structure.

Seebeck coefficients at three (*xx*, *yy*, *zz*) directions slightly deviate, which is in great agreement to the minor anisotropy in experimental measurement. Such deviation may be attributed to the difference between elastic and plastic properties.

In summary, the elastic/plastic and electronic properties of single crystal and polycrystal ZrB_{12} have been studied by experiments and first principle simulations. Under the load of 0.25 and 0.49 N, the Vickers hardness of polycrystalline ZrB_{12} exceeds 40 GPa, suggesting the very hard property at small load. Under the load of 4.9 N, the measured Vickers hardness decreases and saturates at ≈27.0 GPa, which is slightly higher than the well-known ReB_2, WB_3. Revealed by first principle simulations, the ideal shear strength of ZrB_{12} can be as high as 34.5 GPa (B_6O 38.0 GPa) because the frameworks are constructed with very high symmetrical B–B clusters. In addition to the high strength, ZrB_{12} also exhibits superior metallic behavior with ultralow electrical resistivity ≈18 μΩ·cm, and Seebeck coefficient ≈2.0 $\mu V \cdot K^{-1}$ (RT) both of which are comparable to that of Pt. First principle simulations show that the extensive B–B covalent network in ZrB_{12} can form delocalized π-bonds, which generate extensive conducting channels for valence electrons by contacting Zr 4d orbitals. Such delocalized

hybridization of electronic state between valence-bonding framework and doped transition metal provides us an insight to design metallic-hard materials. The combination of excellent mechanical and electrical property of ZrB_{12} can greatly extend the functions in many fields such as hard coatings or anvils of large volume press.

Experimental Section

The ZrB_{12} single crystal was prepared through an inductive zone melting method and the experimental detail could be found in Ref. [37] The polycrystalline ZrB_{12} were synthesized using a high-pressure reaction between Zr and B with the molar ratio at 1:18, pre-mixed homogenously in mortar. Before experiment, a pre-pressed pellet was placed in an MgO capsule, which was then sealed in a graphite heater. At the target pressure of 6 GPa, the temperature was gradually increased to 2300 K, and the sample was soaked for 30 min before quenching to room temperature. The final polycrystalline products were characterized by X-ray diffraction with Cu Kα radiation. The crystal structure was refined based on XRD data using Rietveld refinements and the General Structure Analysis System (GSAS) software.[38] The Vickers hardness was measured using a micro-hardness tester on well-sintered bulk samples under different applied loads of 0.25–4.9 N. In order to increase the fidelity of these measurements, the authors repeated ten times with a dwelling time of 15 s under each load. The final Vickers hardness was obtained from the mean value of the ten data points, with its uncertainty σ determined from $\sigma = \sqrt{\frac{1}{N}\sum_1^N (x_i - x)^2}$ where $N = 10$ in this case, x_i is the hardness value from each individual indentation, and $\overline{x}$ is the mean value of the measured hardness.

High-*P* synchrotron X-ray diffraction experiments using a diamond-anvil cell (DAC) were performed at the Beijing synchrotron radiation facility (BSRF) and Argonne National Lab, Advanced Photon Source (APS)-16BMD. The obtained polycrystalline ZrB_{12} was ground into powders and loaded into the sample hole in a stainless steel gasket with neon as pressure-transmitting medium. A few ruby balls were loaded into the same sample chamber to serve as internal pressure standard. The collected angle-dispersive diffraction data were analyzed by integrating 2D images as a function of 2θ using the program Fit2D to obtain the conventional, 1D diffraction profiles.

The temperature dependence of resistivity along different crystallographic directions was measured with the conventional four-probe method in a commercial physical property measurement system (9T, Quantum Design). The samples were cut into rectangular shape with typical dimensions of 0.5 mm × 0.5 mm × 1 mm, for which the longest dimension is along the designed crystallographic direction. Four golden wires of φ20 µm were attached to the surface of the sample with silver paste, having the excitation current of typical 2 mA passing through the outer two probes while the inner two probes for voltage signal. The resistivity ρ was calculated from the obtained resistance R according to $\rho = R \times S/L$, where S is the cross-section of the sample and L is the distance between the two voltage probes. The Seebeck coefficient was measured with four probe method, with a cold end temperature of 300 K, and the T for hot end range from 300 to 310 K. The potential difference on the samples induced by thermal gradient was recorded by Agilent 34972 A LXI data acquisition, and further used to calculate the Seebeck coefficient.

First principle calculations were performed using the Vienna Ab-Initio Simulation Package (VASP code)[39] with the projector augmented wave method[40] employed to describe the electron–ion interaction and the generalized-gradient approximation of Perdew–Burke–Ernzerhof[41] for the exchange correlation term. The integration in the Brillouin zone had been done on special k points for the phases that were under consideration, which were determined according to the Monkhorst–Pack scheme and the tetrahedron method with Blöchl corrections for the density of states and smearing methods for the stress calculations. In the stress–strain calculations, the crystal symmetry of the crystal under a large strain may be changed and the Brillouin zone significantly deformed. Therefore the authors adopted a high energy cutoff of 600 eV. In the calculations of electronic band structure, the plane-wave energy cutoff was set at 350 eV, and the first Brillouin zone of ZrB_{12} unit cell was sampled by 30 × 30 × 30 Monkhorst-Pack k-mesh.

The Boltzmann transition theory in Wannier90 code was used to calculate the Seebeck coefficient based on the DFT calculated band structure.[42,43] The authors constructed 34 Wannier orbitals for the Zr-d and B-sp^2 hybridization orbitals from a self-consistent calculation. Figure S6a in the Supporting Information shows the excellent agreement between the DFT and Wannier interpolated band structures. Then a dense 100 × 100 × 100 mesh was used to calculate the transport distribution function $\sum(E)$. The corresponding relaxation time $\tau = 10$ fs was chosen.

Supporting Information

Supporting Information is available from the Wiley Online Library or from the author.

Acknowledgements

T.M. and H.L. contributed equally to this work. The authors would like to thank Dr. Jun-Yi Ge for providing the single crystal samples. The synchrotron x-ray diffraction experiments were carried out at BSRF and 16BMD, APS, Argonne National Lab. The authors would like to thank the Fundamental Research Funds for the Central Universities of Beihang University, National Science Foundation of China (51471018 and 51402350), and National Thousand Young Talents Program of China.

Received: July 28, 2016
Revised: September 17, 2016
Published online:

[1] S. Veprek, R. F. Zhang, A. S. Argon, *J. Int. Biomed. Inf. Data* **2011**, *33*, 409.
[2] E. Zhao, J. Meng, Y. Ma, Z. Wu, *Phys. Chem. Chem. Phys.* **2010**, *12*, 13158.
[3] W. G. Fahrenholtz, G. E. Hilmas, I. G. Talmy, J. A. Zaykoski, *J. Am. Ceram. Soc.* **2007**, *90*, 1347.
[4] D. Roundy, M. L. Cohen, *Phys. Rev. B* **2001**, *64*, 212103.
[5] Y. Zhang, H. Sun, C. Chen, *Phys. Rev. B* **2006**, *73*, 144115.
[6] R. B. Kaner, J. J. Gilman, S. H. Tolbert, *Science* **2005**, *308*, 1268.
[7] J. B. Levine, S. H. Tolbert, R. B. Kaner, *Adv. Funct. Mater.* **2009**, *19*, 3519.
[8] R. Mohammadi, A. T. Lech, M. Xie, B. E. Weaver, M. T. Yeung, S. H. Tolbert, R. B. Kaner, *Proc. Natl. Acad. Sci. USA* **2011**, *108*, 10958.
[9] R. F. Zhang, D. Legut, Z. J. Lin, Y. S. Zhao, H. K. Mao, S. Veprek, *Phys. Rev. Lett.* **2012**, *108*, 25502.
[10] H. Gou, N. Dubrovinskaia, E. Bykova, A. A. Tsirlin, D. Kasinathan, W. Schnelle, A. Richter, M. Merlini, M. Hanfland, A. M. Abakumov, D. Batuk, G. V. Tendeloo, Y. Nakajima, A. N. Kolmogorov, L. Dubrovinsky, *Phys. Rev. Lett.* **2013**, *111*, 157002.
[11] A. Knappschneider, C. Litterscheid, D. Dzivenko, J. A. Kurzman, R. Seshadri, N. Wagner, J. Beck, R. Riedel, B. Albert, *Inorg. Chem.* **2013**, *52*, 540.
[12] S. Wang, X. Yu, J. Zhang, Y. Zhang, L. Wang, K. Leinenweber, H. Xu, D. Popov, C. Park, W. Yang, D. He, Y. Zhao, *J. Superhard Mater.* **2014**, *36*, 279.

DOI: 10.1002/adma.201604003

[13] J. W. Simonson, D. Wu, S. J. Poon, S. A. Wolf, *J. Supercond. Novel Magn.* **2010**, *23*, 417.
[14] J. B. Levine, S. L. Nguyen, H. I. Rasool, J. A. Wright, S. E. Brown, R. B. Kaner. *J. Am. Chem. Soc.* **2008**, *130*, 16953.
[15] H. Y. Chung, M. B. Weinberger, J. B. Levine, A. Kavner, J. M. Yang, S. H. Tolbert, R. B. Kaner, *Science* **2007**, *316*, 436.
[16] M. T. Yeung, J. L. Lei, R. Mohammadi, C. L. Turner, Y. Wang, S. H. Tolbert, R. B. Kaner, *Adv. Mater.* **2016**, *28*, 6993.
[17] Q. F. Gu, G. Krauss, W. Steurer, *Adv. Mater.* **2008**, *20*, 3620.
[18] J. Q. Qin, D. W. He, J. H. Wang, L. M. Fang, L. Lei, Y. J. Li, J. Hu, Z. L. Kou, Y. Bi, *Adv. Mater.* **2008**, *20*, 4780.
[19] Q. Tao, D. F. Zheng, X. P. Zhao, Y. L. Chen, Q. Li, Q. Li, C. C. Wang, T. Cui, Y. M. Ma, X. Wang, P. W. Zhu, *Chem. Mater.* **2014**, *26*, 5297.
[20] S. Veprek, *J. Vac. Sci. Technol. A* **1999**, *17*, 2401.
[21] C. P. Zang, H. Sun, C. F. Chen, *Phys. Rev. B* **2012**, *86*, 180101(R).
[22] D. W. He, S. R. Shieh, T. S. Duffy, *Phys. Rev. B* **2004**, *70*, 184121.
[23] D. R. Petrak, R. Ruh, G. R. Atkings, *Am. Ceram. Soc. Bull.* **1974**, *53*, 569.
[24] R. F. Zhang, Z. J. Lin, Y. S. Zhao, S. Veprek, *Phys. Rev. B* **2011**, *83*, 092101.
[25] R. F. Zhang, S. Veprek, A. S. Argon, *Appl. Phys. Lett.* **2007**, *91*, 201914.
[26] G. E. Grechnev, A. E. Baranovskiy, V. D. Fil, T. V. Ignatova, I. G. Kolobov, A. V. Logosha, N. Y. Shitsevalova, V. B. Filippov, O Eriksson, *Low Temp. Phys.* **2008**, *34*, 921.
[27] H. Dong, A. R. Oganov, Q. Wang, S. N. Wang, Z. Wang, J. Zhang, M. M. D. Esfahani, X. F. Zhou, F. Wu, Q. Zhu, *Sci. Rep.* **2016**, *6*, 31288.
[28] R. F. Zhang, X. D. Wen, D. Legut, Z. H. Fu, S. Veprek, E. Zurek, H. K. Mao, *Sci. Rep.* **2016**, *6*, 23088.
[29] B. Joos, M. S. Duesbery, *Phys. Rev. Lett.* **1997**, *78*, 266.
[30] R. Lortz, Y. Wang, S. Abe, C. Meingast, Y. B. Paderno, V. Filippov, A. Junod, *Phys. Rev. B* **2005**, *72*, 024547.
[31] V. A. Gasparov, N. S. Sidorov, I. I. Zver'kova, S. S. Khassanov, M. P. Kulakov, *J. Exp. Theor. Phys.* **2005**, *101*, 98.
[32] L. Han, S. Wang, J. Zhu, S. Han, W. Li, B. Chen, X. Wang, X. Yu, B. Liu, R. Zhang, Y. Long, J. Cheng, J. Zhang, Y. Zhao, C. Jin, *Appl. Phys. Lett.* **2015**, *106*, 221902.
[33] S. Thakur, D. Biswas, N. Sahadev, P. K. Biswas, G. Balakrishnan, K. Maiti, *Sci. Rep.* **2013**, *3*, 3342.
[34] R. Dronskowski, P. E. Bloechl, *J. Phys. Chem.* **1993**, *97*, 8617.
[35] V. L. Deringer, A. L. Tchougréeff, R. Dronskowski, *J. Phys. Chem. A* **2011**, *115*, 5461.
[36] S. Maintz, V. L. Deringer, A. L. Tchougréeff, R. Dronskowski, *J. Comput. Chem.* **2013**, *34*, 2557.
[37] D. Daghero, R. S. Gonnelli, G. A. Ummarino, A. Calzolari, V. Dellarocca, V. A. Stepanov, V. B. Filippov, Y. B. Paderno, *Supercond. Sci. Technol.* **2004**, *17*, S250.
[38] B. H. Toby, *J. Appl. Cryst.* **2001**, *34*, 210.
[39] G. Kresse, J. Furthmüller, *Comput. Mater. Sci.* **1996**, *6*, 15.
[40] G. Kresse, J. Joubert, *Phys. Rev. B* **1999**, *59*, 1758.
[41] J. P. Perdew, K. Burke, M. Ernzerhof, *Phys. Rev. Lett.* **1996**, *77*, 3865.
[42] A. A. Mostofi, J. R. Yates, Y. S. Lee, I. Souza, D. Vanderbilt, N. Marzari, *Comput. Phys. Commun.* **2008**, *178*, 685.
[43] G. Pizzi, D. Volja, B. Kozinsky, M. Fornari, N. Marzari, *Comput. Phys. Commun.* **2014**, *185*, 422.